

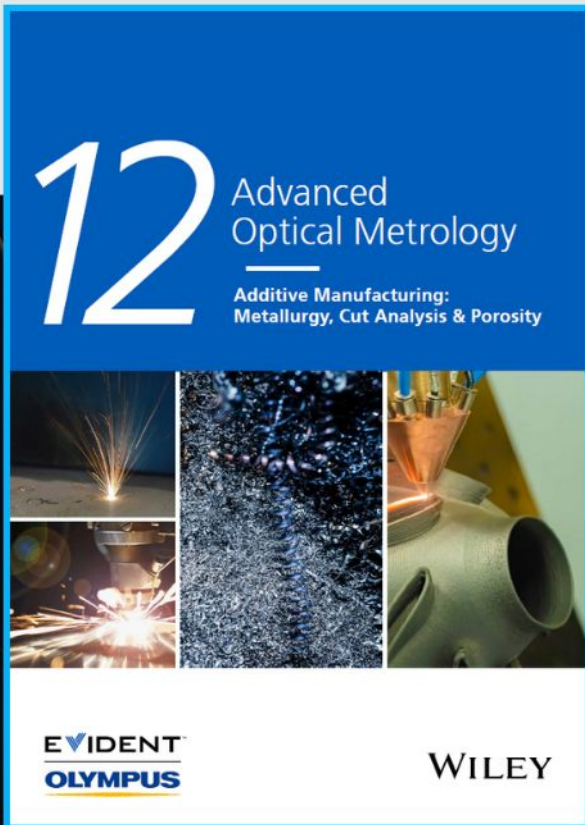
ULRR

Lithiophilic nanowire guided Li deposition in Li metal batteries

Item Type	Article
Authors	Ahad, Syed Abdul;Bhattacharya, Shayon;Kilian, Seamus;Ottaviani, Michela;Ryan, Kevin M.;Kennedy, Tadhg;Thompson, Damien;Geaney, Hugh
Citation	Small, 2205142
Publisher	Wiley-VCH GmbH
Download date	2026-05-15 11:30:05
Item License	https://creativecommons.org/licenses/by-nc-sa/4.0/
Link to Item	https://doi.org/10.34961/researchrepository-ul.21666344



Additive Manufacturing: Metallurgy, Cut Analysis & Porosity



The latest eBook from
Advanced Optical Metrology.
Download for free.

In industry, sector after sector is moving away from conventional production methods to additive manufacturing, a technology that has been recommended for substantial research investment.

Download the latest eBook to read about the applications, trends, opportunities, and challenges around this process, and how it has been adapted to different industrial sectors.

EVIDENT™
OLYMPUS

WILEY

Lithiophilic Nanowire Guided Li Deposition in Li Metal Batteries

Syed Abdul Ahad, Shayon Bhattacharya, Seamus Kilian, Michela Ottaviani, Kevin M. Ryan, Tadhg Kennedy, Damien Thompson, and Hugh Geaney*

Lithium (Li) metal batteries (LMBs) provide superior energy densities far beyond current Li-ion batteries (LIBs) but practical applications are hindered by uncontrolled dendrite formation and the build-up of dead Li in “hostless” Li metal anodes. To circumvent these issues, we created a 3D framework of a carbon paper (CP) substrate decorated with lithiophilic nanowires (silicon (Si), germanium (Ge), and SiGe alloy NWs) that provides a robust host for efficient stripping/plating of Li metal. The lithiophilic $\text{Li}_{22}\text{Si}_5$, $\text{Li}_{22}(\text{Si}_{0.5}\text{Ge}_{0.5})_5$, and $\text{Li}_{22}\text{Ge}_5$ formed during rapid Li melt infiltration prevented the formation of dead Li and dendrites. $\text{Li}_{22}\text{Ge}_5/\text{Li}$ covered CP hosts delivered the best performance, with the lowest overpotentials of 40 mV (three times lower than pristine Li) when cycled at $1 \text{ mA cm}^{-2}/1 \text{ mAh cm}^{-2}$ for 1000 h and at $3 \text{ mA cm}^{-2}/3 \text{ mAh cm}^{-2}$ for 500 h. Ex situ analysis confirmed the ability of the lithiophilic $\text{Li}_{22}\text{Ge}_5$ decorated samples to facilitate uniform Li deposition. When paired with sulfur, LiFePO_4 , and NMC811 cathodes, the CP-LiGe/Li anodes delivered 200 cycles with 82%, 93%, and 90% capacity retention, respectively. The discovery of the highly stable, lithiophilic NW decorated CP hosts is a promising route toward stable cycling LMBs and provides a new design motif for hosted Li metal anodes.

1. Introduction


The re-emergence of Lithium (Li) metal batteries (LMBs) during the last decade has been driven by the performance saturation

S. Abdul Ahad, S. Bhattacharya, S. Kilian, M. Ottaviani, K. M. Ryan, T. Kennedy, D. Thompson, H. Geaney

Bernal Institute
University of Limerick
Limerick V94 T9PX, Ireland
E-mail: hugh.geaney@ul.ie

S. Abdul Ahad, S. Kilian, M. Ottaviani, K. M. Ryan, T. Kennedy, H. Geaney
Department of Chemical Sciences
University of Limerick
Limerick V94 T9PX, Ireland

S. Bhattacharya, D. Thompson
Department of Physics
University of Limerick
Limerick V94 T9PX, Ireland

 The ORCID identification number(s) for the author(s) of this article can be found under <https://doi.org/10.1002/smll.202205142>.

© 2022 The Authors. Small published by Wiley-VCH GmbH. This is an open access article under the terms of the Creative Commons Attribution-NonCommercial-NoDerivs License, which permits use and distribution in any medium, provided the original work is properly cited, the use is non-commercial and no modifications or adaptations are made.

DOI: 10.1002/smll.202205142

of state-of-the-art LIBs using graphite anodes.^[1–3] Li metal is considered the ideal anode material with advantages including the highest theoretical capacity (3860 mAh g^{-1}), extremely low density (0.53 g cm^{-3}), and low redox potential (-3.04 V vs standard hydrogen electrode). With such attractive features, Li metal is a promising candidate to substitute LIB anodes to meet the rising demand for higher energy density (ED) storage for transport, environmental monitoring, and electricity grid applications among others.^[4,5,6] Rapid development of Li metal anodes would also benefit emerging high ED systems such as Li-S and Li-O₂ batteries that provide high theoretical ED of 2600 and 3500 Wh kg⁻¹ respectively.^[7,8] To date, LMB development has been plagued by major performance issues^[9,10] including Li dendrite formation which occurs due to inhomogeneous Li-ion flux distribution on the Li metal surface during repeated stripping/plating cycles. The dendrites can

pierce the separator, causing the cell to short circuit, posing a risk of dangerous overheating. Even in cases where catastrophic failure does not occur, uneven Li dissolution contributes to the formation of “dead Li”, decreasing the overall efficiency of the anode.^[11,12] Another challenge is the formation of an unstable solid electrolyte interface (SEI) on the Li surface, which breaks and re-forms due to volume fluctuations caused by the Li stripping and plating process.^[13,14] This results in excess electrolyte consumption, causing high overpotentials with low coulombic efficiencies during the charge/discharge process.^[3,4,15]

Several strategies have been proposed to overcome issues in Li-metal anodes such as modification of electrolytes to promote uniform Li deposition, using different salts and salt concentrations,^[16–18] additives,^[19,20] fluorinated solvents^[21–23] and (quasi) solid state electrolytes^[24,25] as well. Another strategy involves the formation of artificial SEI layers that can limit electrolyte consumption.^[26–29] However, to overcome the volumetric changes of the Li metal anode, electrolyte and SEI modifications are not enough. In response, strategies such as the use of foreign hosts, e.g., metal foams, carbon, and graphene,^[30–33] have been explored to avoid the formation of dead Li and to accommodate volumetric stresses. To further improve the lithiophilicity of the hosts, lithiophilic coatings of metal and metal oxides/sulfides/fluorides have been used to homogenize the Li-ion flux on the Li metal surface to avoid dendrite formation.^[34–39]

Here, we used atomic and molecular-level design to advance beyond previous strategies, achieving dramatically improved LMBs by decorating 3D carbon paper (CP) current collectors with highly lithiophilic silicon (Si), SiGe, or germanium (Ge) nanowires (NWs) grown via a solvent-vapor growth technique (SVG). When lithiated and coated with excess Li, the lithiophilic NWs regulated the Li-ion flux by minimizing the local current density on the surface of the Li anode, promoting uniform Li deposition.^[30,32,40] This beneficial effect of the lithiophilic NWs within the 3D anode host is clearly demonstrated by control experiments, wherein the parent CP (without any NWs) was shown to be highly lithiophobic, not allowing any Li infiltration. The Li-infilled 3D CP-NW substrates have several benefits compared to “hostless” Li such as i) providing mechanical and electrical support to infused Li during stripping/plating, ii) the NW morphology provides uniform localized current density to avoid dendrite formation and iii) the “lithiophilic” phases formed (Li_xSi , Li_xSiGe , Li_xGe) provide additional support for uniform Li deposition during stripping/plating. The formation of lithiated-Si, SiGe, and Ge alloys promotes uniform Li deposition on the 3D carbon substrate as visualized using scanning electron microscopy (SEM) analysis, supported by extensive electrochemical characterization and density functional theory (DFT) calculations. This unique 3D hierarchical structure containing lithiophilic NWs, provided the most stable performance in the CP-LiGe/Li anode at 1 mA cm^{-2} and 3 mA cm^{-2} for hundreds of hours (1000 h and 500 h respectively) with overpotentials as low as 40 mV, three times lower than that of a pristine Li anode. Examination of the CP-LiSi/Li, CP-LiSiGe/Li, and CP-LiGe/Li anodes, post Li infiltration and electrochemical cycling with sulfur, LiFePO_4 , and NMC811 cathodes, showed the most uniform Li deposition/stripping (without dendrite formation) for CP-LiGe/Li.

2. Results and Discussion

2.1. Fabrication of Lithiophilic NW/CP Composite Anode

The lithiophilic NW-CP substrate at each stage of the fabrication process is shown in **Figure 1a**. Briefly, heat-treated carbon paper (I) was coated with tin (Sn) catalyst seeds for NW growth. The Sn seeds were deposited using tin chloride (SnCl_2) electroplating solution via a pulsed electrodeposition process (II). Once coated with Sn seeds, SVG was used to grow Si, SiGe ($\text{Si}_{0.5}\text{Ge}_{0.5}$) and Ge NWs on CP (III) followed by a heat treatment to improve the lithiophilicity of the NW substrates (full experimental details are in Supporting information-SI). Optical photographs of different substrates showing color changes during each fabrication step of NW growth are given in **Figure 1b**. These CP-based substrates were successfully decorated with lithiophilic NWs and later used as Li hosts. The SEM analysis of bare CP and Sn-CP shows a network of carbon fibers woven together with uniform deposition of Sn seed (**Figure S1a,b**, Supporting Information). The SEM data presented in **Figure 1c,d,e** provides a comparison of Si, SiGe, and Ge NW growth on CP substrate. It is evident that the NWs have formed a dense network, fully covering the carbon scaffold with NW mass loadings in the range of $0.8\text{--}1.1 \text{ mg cm}^{-2}$.

The Si, SiGe, and Ge NWs have indicative diameters of 300 nm, 310 nm, and 390 nm respectively.

X-ray diffraction (XRD) analysis of CP, CP-Sn, CP-Si, CP-SiGe, and CP-Ge NW highlighted the compositional changes of the different substrates during the synthesis (**Figure 1f**). The major reflections from CP and Sn remain present in all the NW-coated CP substrates. Confirmation of the growth of Si and Ge phase is evident with the presence of major (111) reflections at 28.3° and 27.2° respectively, also matching well with standard patterns for Si and Ge. The SiGe ($\text{Si}_{0.5}\text{Ge}_{0.5}$) NWs major (111) reflection lies between that of Si and Ge at 27.7° (**Figure S2**, Supporting Information).^[41,42] Additionally, the energy dispersive X-ray spectroscopy (EDX) analysis of SiGe alloy NWs further confirms a $\approx 50:50$ atomic ratio of Si: Ge in the SiGe alloy NWs (**Figure S3**, Supporting Information). Across the three compositions, the Si, SiGe and Ge NWs demonstrate a core-shell structure with a crystalline core and an oxide shell post fabrication. The oxide shell thickness varies from ~ 25 to 35 nm for all the compositions (**Figure S4a,c,e**, Supporting Information, **inset**). The SEM images (**Figure S4b,d,f**, Supporting Information) confirm the presence of a uniform outer layer with a different contrast from the inner NW core. The corresponding EDX mapping demonstrates that the O signal is concentrated on the outer periphery of the NWs. The signals from Si and/or Ge are uniform throughout the cores, suggesting uniform composition of the phases formed. To analyse the nature of the oxide shell, X-ray photoelectron spectroscopy (XPS) was conducted. The Si 2p and Ge 3d spectra suggest the presence of Si-oxide (103.3 eV) for the Si and SiGe NWs and Ge-oxide (33.1 eV) on the surface of the Ge and SiGe NWs (**Figure S5a,b**, Supporting Information). We find no evidence for Si and Ge oxide segregation on the surface of the SiGe NWs. The corresponding O 1s and Sn 3d spectra also suggest the formation of Sn-oxide ($486.5 \text{ eV} - \text{Sn } 3d$) (**Figure S5c,d**, Supporting Information). The C 1s spectra confirms the presence of typical carbon moieties such as $\text{O}-\text{C}=\text{O}$, $\text{C}-\text{O}$, $\text{C}-\text{C}$, and $\text{C}\equiv\text{C}$ across all the samples (**Figure S5e**, Supporting Information).^[43,44] The XPS analysis did not reveal the presence of any crystalline peaks from Si or Ge as the oxide layer thickness $\approx 25\text{--}35 \text{ nm}$ is beyond the detection limit of XPS.

The Li infusion step was carried out by brief contact of the NW-coated CP substrates with molten Li at 350°C inside an Ar glovebox (**Figure 2a**). The molten Li infused into the CP-Si, CP-SiGe, and CP-Ge NW substrate within seconds (**Movie S1**, Supporting Information). By contrast, molten Li did not infiltrate bare carbon paper (**Movie S2**, Supporting Information). This clearly demonstrates the benefits of coating CP with lithiophilic Si, SiGe, and Ge NWs. The Li infiltrated samples are henceforth labeled as CP-LiSi/Li, CP-LiSiGe/Li, and CP-LiGe/Li for brevity. The SEM images of Li infiltrated substrates show uniform Li infiltration on the NW-coated CP substrates as well as lithiated NWs (**Figure 2b,c,d-i**). The inset photographs show the substrates covered with shiny metallic Li after infiltration. The lithiated NWs coated with Li metal show significant swelling, with larger diameters in the range of $\approx 650\text{--}800 \text{ nm}$. It is also evident that the underlying NW morphology is retained after Li infiltration and the NWs remain bound to the CP scaffold (**Figure 2b,c,d-ii**). Cross-sectional examination of these samples shows the average thickness of the Li infiltrated

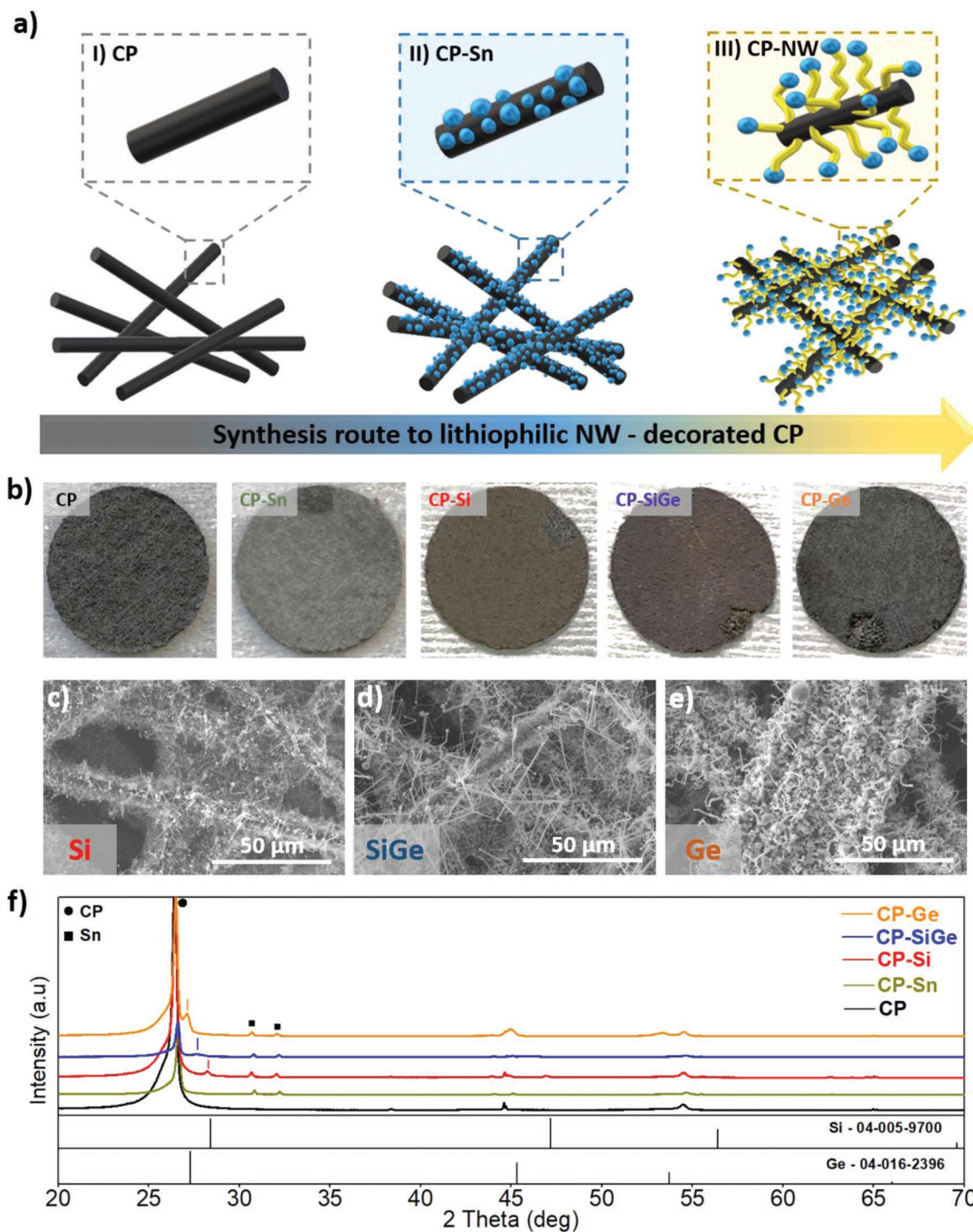


Figure 1. Synthesis and phase characterization of different NW-coated CP substrates (CP-Si, CP-SiGe, CP-Ge). a) Schematic illustration of the steps involved in the synthesis process of Si, SiGe alloy and Ge NWs coated CP substrates. b) Photographic images of steps involved in the fabrication of NW-coated CP substrates (substrate area: 0.71 cm²). SEM images of c) CP-Si d) CP-SiGe and e) CP-Ge. f) XRD analysis of CP, CP-Sn, CP-Si, CP-SiGe, and CP-Ge NWs between 20° and 70° with the corresponding standard patterns of pure Si and pure Ge phases.

substrates to be $\approx 370 \mu\text{m}$ (Figures 2b,c,d-iii) as compared to $240 \mu\text{m}$ for the bare CP prior to Li infiltration (Figure S6a, Supporting Information). The cross-sectional view (Figure 2-iii) confirms complete Li infiltration throughout the substrates, suggesting robust lithiophilic properties of the NWs which

facilitated uniform Li infiltration throughout the entire carbon paper. XRD analysis of the Li-infiltrated substrates mapped the phase changes after the reaction with molten Li. The common phases present among all the three compositions of CP-LiSi/Li, CP-LiSiGe/Li, and CP-LiGe/Li are LiC₆, LiC₁₂, and Li metal

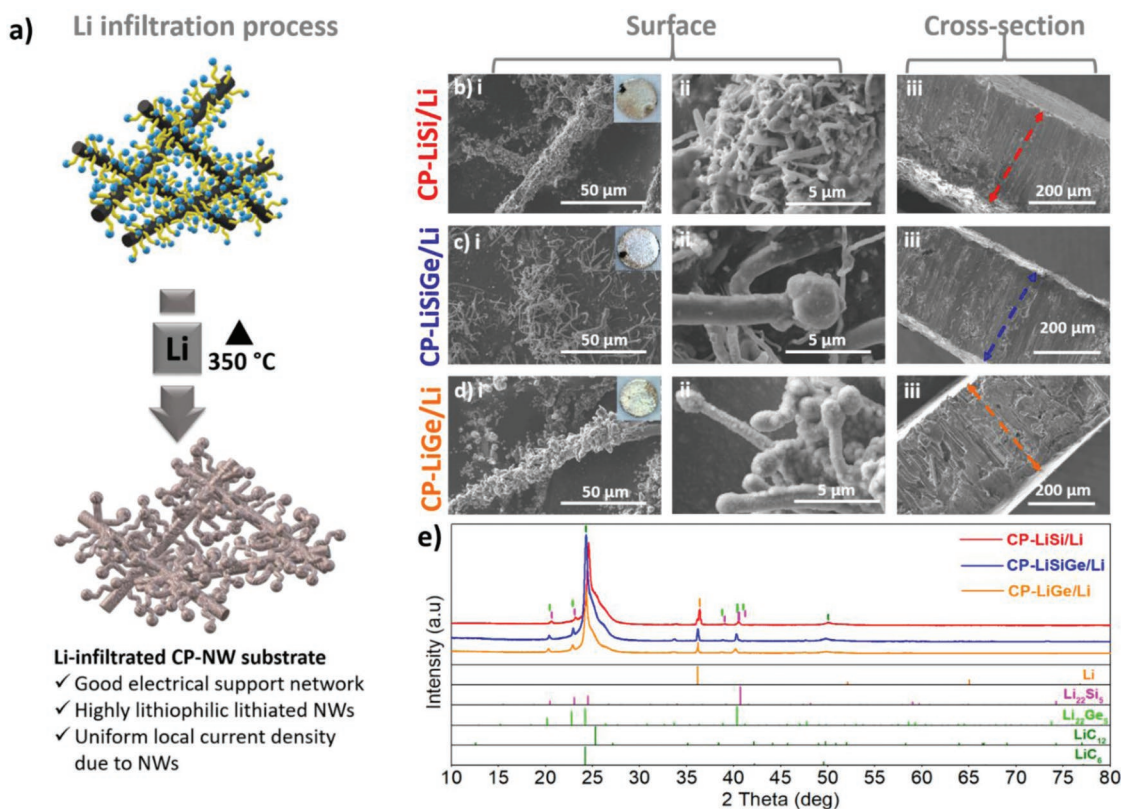
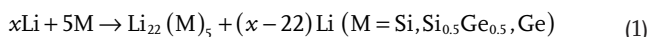


Figure 2. Morphological and phase analysis of different metal anode NW (CP-LiSi/Li, CP-LiSiGe/Li, CP-LiGe/Li) substrates post reaction with molten Li and infiltration. a) Schematic illustration of the transformation of lithiophilic NW substrate to Li infiltrated NW substrate using molten Li approach. SEM images of b) CP-LiSi/Li c) CP-LiSiGe/Li d) CP-LiGe/Li NWs substrates representing (i, ii) surface and (iii) cross-sectional morphologies. e) XRD analysis of CP-LiSi/Li, CP-LiSiGe/Li, and CP-LiGe/Li NW substrates between 10° and 80° with the corresponding standard patterns of pure Li (JCPDS no. 01-071-6176), $\text{Li}_{22}\text{Si}_5$ (JCPDS no. 01-077-2882), $\text{Li}_{22}\text{Ge}_5$ (JCPDS no. 01-081-6059), LiC_{12} (JCPDS no. 01-085-9951) and LiC_6 (JCPDS no. 04-002-4997).

(Figure 2e). This suggests that during Li infiltration, some CP also reacts with Li to form lithiated carbide phases such as LiC_6 and LiC_{12} .^[45,46] Shoulder peaks from the underlying CP are also evident in Figure S6b, Supporting Information. Most importantly, during the reaction with Li, the Si, SiGe, and Ge NWs convert to their lithiated phases $\text{Li}_{22}\text{Si}_5$, $\text{Li}_{22}(\text{Si}_{0.5}\text{Ge}_{0.5})_5$, and $\text{Li}_{22}\text{Ge}_5$, with reactions proceeding according to Equation 1 below:



Moving from $\text{Li}_{22}\text{Si}_5$ to $\text{Li}_{22}\text{Ge}_5$, the XRD reflections shifted toward lower angle, as also seen above for pristine Si, SiGe, and Ge NWs (Figure 1f and Figures S7a,b, Supporting Information), with $\text{Li}_{22}(\text{Si}_{0.5}\text{Ge}_{0.5})_5$ intermediate between $\text{Li}_{22}\text{Si}_5$ and $\text{Li}_{22}\text{Ge}_5$. No peak splitting was observed in the phase analysis of $\text{Li}_{22}(\text{Si}_{0.5}\text{Ge}_{0.5})_5$ which suggests that no phase segregation into $\text{Li}_{22}\text{Si}_5$ and $\text{Li}_{22}\text{Ge}_5$ occurred during the reaction between SiGe alloy NWs and Li metal. Due to the presence of Sn catalyst and high lithiophilicity of Sn,^[47] it is possible that LiSn alloy may form during Li infusion. The peaks from LiSn alloy are not clearly visible in the XRD analysis and may have been masked by high intensities of LiC_6 and Li_{22}X_5 ($\text{X} = \text{Si}, \text{SiGe}, \text{Ge}$) formed. However, a similar lithiophilic effect (of Sn) is expected in all the different anodes (i.e., CP-LiSi/Li,

CP-LiSiGe/Li, and CP-LiGe/Li) due to the constant loading of Sn seed (0.07 mg cm^{-2}) used to grow Si, SiGe, and Ge NWs. To determine the amount of stored Li inside the substrates, Li was fully stripped out from the CP-LiSi/Li, CP-LiSiGe/Li, and CP-LiGe/Li substrates using an upper voltage cut-off of 1.5 V. The resulting Li areal capacities were in the range of $36\text{--}43 \text{ mAh cm}^{-2}$ (Figure S8a, Supporting Information). Within this electrochemical data, a common delithiation feature $\approx 0.5 \text{ V}$ confirmed delithiation of the lithiated Si, SiGe, and Ge phases. This feature was only seen after all the Li metal had been stripped out, indicating that the lithiated phases can be retained during lower capacity stripping required for standard anodes. It is evident from comparing the pre-stripping and post-stripping cross-sectional images of the substrates that all the Li has been stripped out at 1.5 V while the porous structure was retained (Figure S8b, Supporting Information).

2.2. Symmetric Cell Performance of Li, CP-LiSi/Li, CP-LiSiGe/Li, and CP-LiGe/Li Hosts

The Symmetric cells were assembled using matched electrodes ($\text{Li} \parallel \text{Li}, \text{CP-LiSi/Li} \parallel \text{CP-LiSi/Li}, \text{CP-LiSiGe/Li} \parallel \text{CP-LiSiGe/Li}$ and $\text{CP-LiGe/Li} \parallel \text{CP-LiGe/Li}$) and Li^+ solvated ether-based electrolyte (1 M LiTFSI in DOL:DME). At a current density of

1 mA cm⁻² with a stripping/plating capacity of 1 mAh cm⁻², the Li symmetric cell short-circuited after ≈200 h, due to excessive consumption of electrolyte and dendrite formation.^[34,48] Relative to Li metal, the Li infiltrated substrates (i.e., CP-LiSi/Li, CP-LiSiGe/Li, CP-LiGe/Li) delivered substantially better performance (Figure 3a). It was found that the overpotential of the Li infiltrated substrates gradually increased over time, with the CP-LiGe/Li delivering the most stable performance of over 1000 h as compared to CP-LiSiGe/Li and CP-LiSi/Li symmetric cells. The difference in overpotential among different substrates is depicted in Figure 3a (insets) and Figure 3b. Initially, the Li symmetric cell had the highest overpotential of 55 mV followed by CP-LiSi/Li (40 mV), CP-LiSiGe/Li (40 mV), and CP-LiGe/Li (37 mV). The Li overpotential increased to 135 mV after 400 h while the overpotential of CP-LiSi/Li increased to 150 mV after 700 h and CP-LiSiGe/Li increased to 111 mV after 800 h. However, the overpotential of CP-LiGe/Li substrate remained stable at 39 mV up to 1000 h. Monitored over the full course of cycling, the overpotentials remained highest for Li, followed by CP-LiSi/Li and CP-LiSiGe/Li, while the lowest values were seen for CP-LiGe/Li. This suggests that the highly lithiophilic nature of LiGe NWs in CP-LiGe/Li substrate provided stable high-performance stripping/plating in comparison to the relatively less lithiophilic LiSi and LiSiGe NW substrates.^[47] Electrochemical impedance spectroscopy (EIS) was performed to determine the interfacial resistance of symmetric cells during cycling. The EIS analysis (Figure S9, Table S1, Supporting Information) revealed that pristine Li had the highest R_{ct} after 1st cycle followed by CP-LiSi/Li anode. The R_{ct} significantly decreased in CP-LiSiGe/Li anode while the lowest R_{ct} was observed in CP-LiGe/Li anode. Similarly, after 50 cycles the R_{ct} of Li increases, reflecting increased charge transfer resistance due to unstable SEI formation and poor interfacial kinetics whereas CP-LiGe/Li delivered the lowest R_{ct} among the NW-CP anodes. The lowest R_{ct} in CP-LiGe/Li is a testament to a stable SEI formation with fast interfacial kinetics during stripping/plating cycles.^[49,50] Here it is important to mention that in comparison to pristine Li, all the CP-NW substrates performed exceptionally well due to the NW morphology and also due to the general lithiophilic nature of Si, SiGe, or Ge NWs. Additionally, a 300-times greater Li diffusion coefficient of Li in Ge (6.25×10^{-12} cm² s⁻¹) as compared to Si (1.9×10^{-14} cm² s⁻¹) promotes faster Li transport kinetics in Ge, thereby significantly decreasing the chances of dendrite formation in LiGe/Li as compared to LiSiGe/Li and LiSi/Li anodes.^[12,51–53]

Rate capability testing was conducted by varying the current density from 0.5, 1, 2, and 3 mA cm⁻² with a fixed plating capacity of 1 mAh cm⁻² (Figure 3c). The results show that CP-LiGe/Li maintains the lowest overpotentials up to 3 mA cm⁻², unlike the other metal anode compositions. The data shows that the pure Li anode quickly fails at 2 mA cm⁻² while CP-LiSi/Li and CP-LiSiGe/Li also start to exhibit non-uniform stripping behavior at 2 mA cm⁻² which became more prominent at 3 mA cm⁻² (Figure S10, Supporting Information). However, all metal anode substrates except Li recovered well when the current density was returned to 0.5 mA cm⁻². The CP-LiGe/Li also delivers stable performance at high current density of 3 mA cm⁻² at 1 mAh cm⁻² (Figure S11a, Supporting

Information) for 500 h as well as at high plating capacity of 3 mAh cm⁻² at a fixed current density of 1 mA cm⁻² for up to 1000 h (Figure S11b, Supporting Information). In addition, a CP-LiGe/Li symmetric cell was tested at high plating capacity (3 mAh cm⁻²) and high current density (3 mA cm⁻²), and contrasted with a Li symmetric cell. The CP-LiGe/Li symmetric cell shows robust performance up to 500 h whereas the Li symmetric cell shows high overpotential and unstable performance due to dendrite formation and fast electrolyte consumption (Figure 3d). This symmetric cell performance is more stable than most of the previously published literature on carbon paper hosted Li metal anodes (Table S2, Supporting Information) and impressive full-cell performance characteristics are demonstrated in Section 2.5. To determine the compatibility of the hosted anodes for different electrolyte systems, the Li-infiltrated substrates were tested in a carbonate-based electrolyte (1 M LiPF₆ in EC:DEC:EMC). As shown in Figure S12, Supporting Information, CP-LiSi/Li and CP-LiSiGe/Li begin to have higher overpotentials as compared to CP-LiGe/Li post 200 h, with the CP-LiGe/Li substrate again maintaining the lowest overpotentials among all the samples tested up to 1000 h. The symmetric cell testing demonstrates the importance of lithiophilic host composition in maintaining stable Li stripping/plating performance.

2.3. Morphological Evolution of Cycled Anodes

The morphological impact of Li stripping/plating was examined to investigate surface and cross-sectional changes after 50 cycles (Figure 4). In the stripped state after cycling, the CP-LiSi/Li, CP-LiSiGe/Li, and CP-LiGe/Li substrates still showed the presence of NWs, similar to the original samples. However, it is noticeable that the feature size of the Li-infilled, lithiated NWs along with excess Li decreased from CP-LiSi/Li toward CP-LiGe/Li (Figure 4a,b,c). This could be due to a more uniform stripping behavior from the most lithiophilic LiGe containing samples as compared to LiSiGe or LiSi containing samples. The NW morphology is more obvious in Figures 4a,b,c (insets). Cross-sectional analysis of the substrates revealed a relatively smooth surface of the CP-LiGe/Li and CP-LiSiGe/Li compared to a patchy and non-uniform layer on the CP-LiSi/Li surface, which could be due to LiSi having the least lithiophilic nature of the compositions tested (Figure S13a-c, Supporting Information). Similarly, in the plated state (Figures 4d,e,f), it can be observed that the surface features change considerably as compared to the stripped state. After plating, a more uniform Li layer appeared on the surface of samples with CP-LiGe/Li, displaying a flat nanostructured layer of Li metal as compared to the more lumpy appearance on the CP-LiSi/Li substrate (Figures 4d,e,f (insets)). Overall, the uniform Li deposition relates well with the lithiophilic nature of Li₂₂X₅ (x = Si, SiGe, and Ge) phases and the NW morphology which helped to promote uniform Li-ion flux due to high surface area of the NWs.^[30,32] The cross-sectional images after the plating step also confirm uniform Li deposition in the CP-LiGe/Li, indicating its more lithiophilic nature with surface-Li interactions out-competing bulk Li-Li interactions (Figure S13d–f, Supporting Information).

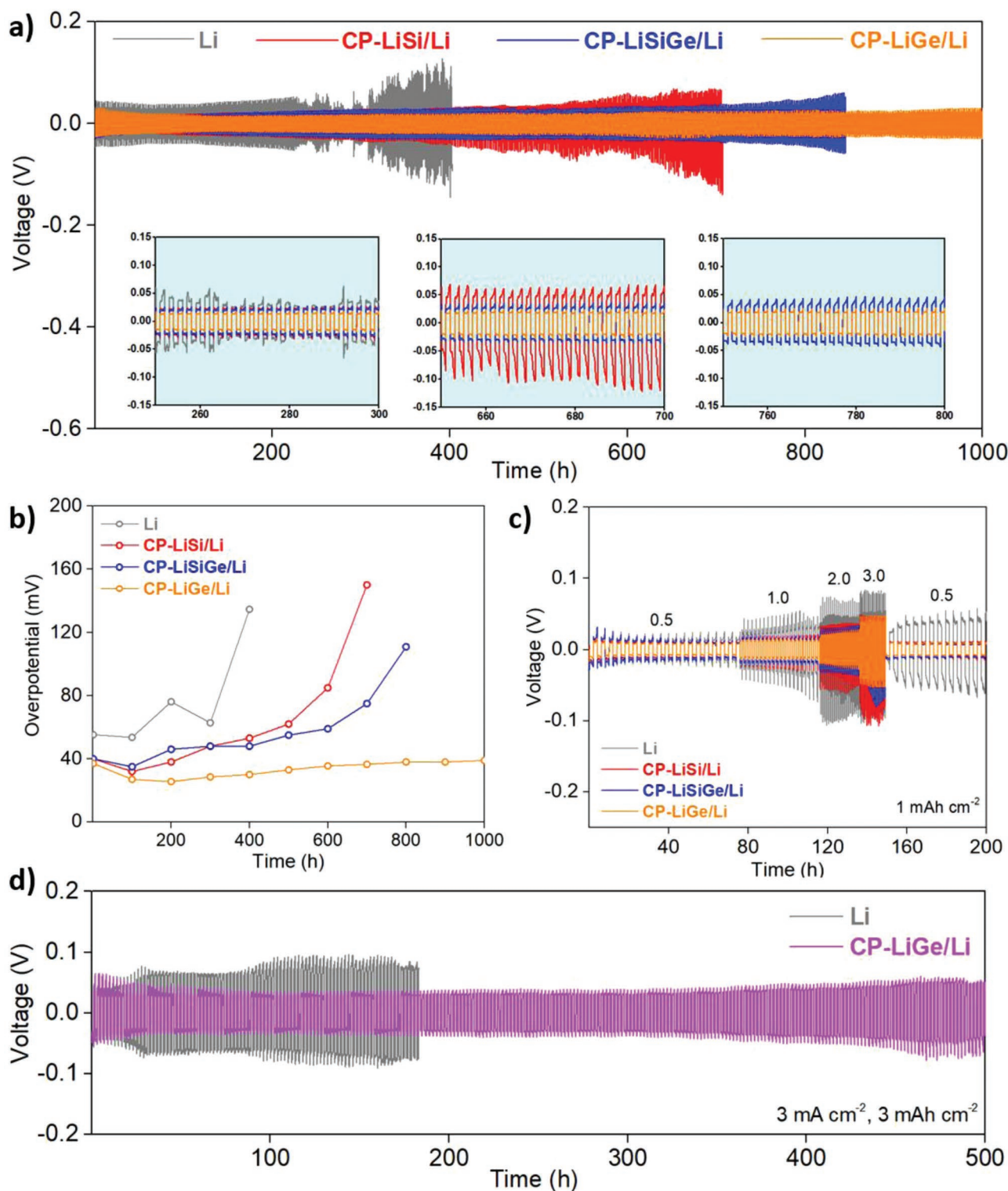


Figure 3. Electrochemical performance of different metal anode NW (CP-LiSi/Li, CP-LiSiGe/Li, CP-LiGe/Li) substrates in symmetric cells. a) Cyclic performance at 1 mA cm^{-2} , 1 mAh cm^{-2} . The insets show voltage – time profiles at various time during cycling. b) Corresponding overpotential versus time profile, c) rate capability tests at 0.5, 1, 2, and 3 mA cm^{-2} at 1 mAh cm^{-2} of Li, CP-LiSi/Li, CP-LiSiGe/Li, and CP-LiGe/Li. d) Symmetric cell cyclic performance at high current density (3 mA cm^{-2}) and plating capacity (3 mAh cm^{-2}).

The stripping/plating behavior phenomena is schematically illustrated, demonstrating uniform Li deposition on high

surface area Li infiltrated, lithiated NW substrates (Figure S14, Supporting Information). The cycled anodes have taken out

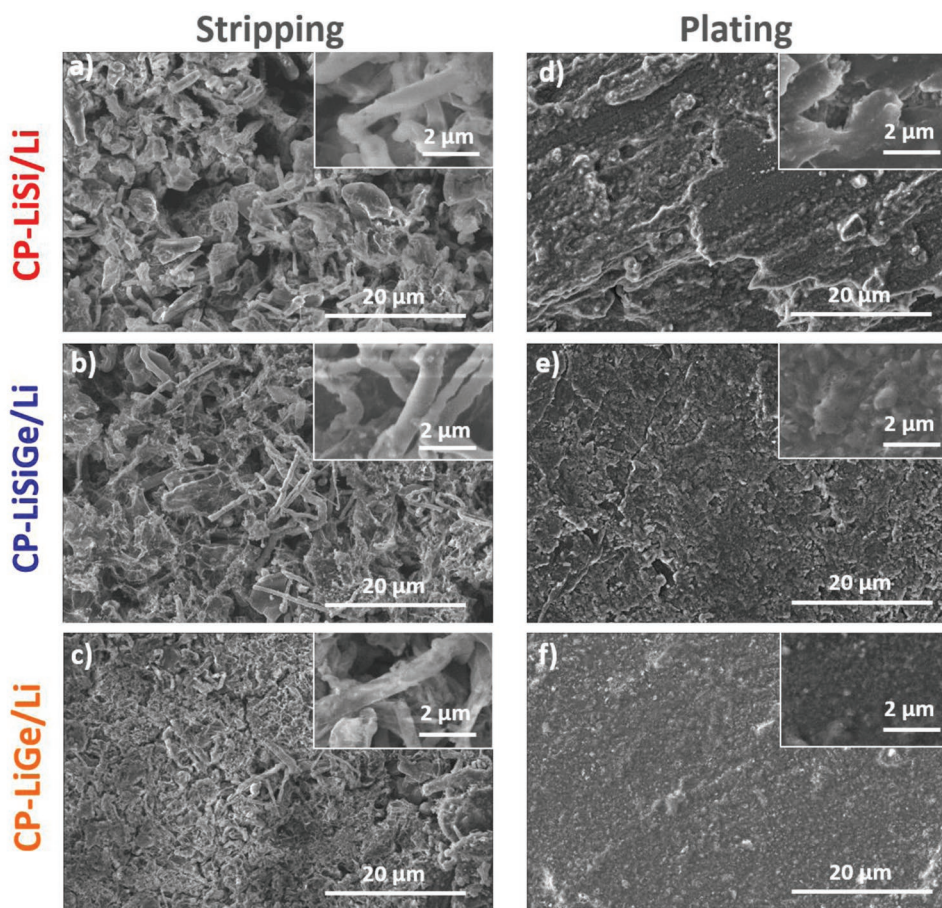


Figure 4. Morphological evolution of different metal anode NW (CP-LiSi/Li, CP-LiSiGe/Li, CP-LiGe/Li) substrates in cycled symmetric cells. SEM analysis of a,d) CP-LiSi/Li, b,e) CP-LiSiGe/Li, and c,f) CP-LiGe/Li substrates after stripping and plating steps post 50 cycles at a current density of 1 mA cm^{-2} .

from the symmetric cells after 50 stripping/plating cycles show no breakage which signifies the mechanical robustness of synthesized anodes (Figure S15, Supporting Information). The pure Li metal cycled electrode shows non-uniform Li deposition across the surface. After just 50 cycles, a layer of dead Li with significant cracks and Li dendrite (Figure S16 – inset) formation among the cracks was evident which causes the Li anode to fail quickly (Figures S16a-c, Supporting Information). XRD analysis of CP-LiSi/Li, CP-LiSiGe/Li, and CP-LiGe/Li substrates post 50 cycles (stripped state – 1 mAh cm^{-2}) demonstrated that the lithiated phases (*i.e.*, $\text{Li}_{22}\text{Si}_5$, $\text{Li}_{22}(\text{Si}_{0.5}\text{Ge}_{0.5})_5$ and $\text{Li}_{22}\text{Ge}_5$) are preserved during the Li stripping/plating process; highlighting their role in guiding uniform Li deposition during cycling (Figure S17, Supporting Information).

2.4. Calculated lithiophilicity of $\text{Li}_{22}\text{Si}_5$, $\text{Li}_{22}(\text{Si}_{0.5}\text{Ge}_{0.5})_5$ and $\text{Li}_{22}\text{Ge}_5$ from density functional theory (DFT) models

To substantiate the apparent higher lithiophilicity of Ge compared to Si in the experiments and probe the atomic level details of the surface interactions, we predicted the binding energy (E_b) between a Li atom and $\text{Li}_{22}\text{Si}_5$ or $\text{Li}_{22}(\text{Si}_{0.5}\text{Ge}_{0.5})_5$ or $\text{Li}_{22}\text{Ge}_5$ using periodic density functional theory (DFT) calculations with the Vienna Ab initio Simulation Package (VASP)

code.^[54,55] A total of five Li binding sites on (110) surfaces of $\text{Li}_{22}\text{Si}_5$, $\text{Li}_{22}(\text{Si}_{0.5}\text{Ge}_{0.5})_5$, and $\text{Li}_{22}\text{Ge}_5$ were considered (Figure S18 a, Supporting Information). Further, four Li binding sites (Figure S18 h, Supporting Information) were also investigated to determine Li adsorption behavior on the (001) surface of the additional LiC_6 phase detected in the XRD characterizations. The binding energy data shows that Li adsorption sites on the lithiated Si, SiGe, and Ge NWs are more favorable than Li adsorption sites on lithiated carbide phase in LiC_6 (Figure S18, Supporting Information). Our surface binding calculations reveal that $\text{Li-Li}_{22}\text{Ge}_5$ produces a more stable Li binding energy (E_b , -2.333 eV) than both $\text{Li-Li}_{22}(\text{Si}_{0.5}\text{Ge}_{0.5})_5$ (-2.261 eV) and $\text{Li-Li}_{22}\text{Si}_5$ (-2.195) (Figure 5a–d), giving $\approx 70 \text{ meV}$ (corresponds to kT at 500 K) preference for Ge versus Si in line with the measured superior stripping/plating ability of the most lithiophilic Ge NWs in the CP-LiGe/Li cells. This is supported by our computed charge density difference maps showing restructuring of the surface electronic structure with bound Li on surface by forming new Li–Si and Li–Ge bonds (see Figure S19a–f, Supporting Information). Furthermore, the projected density of states (PDOS) reveals that bound Li and its surface binding atoms contribute to densities, particularly in the range of ≈ -0.4 to -0.3 eV at the top of the valence band (Figure S19g–i, Supporting Information), reflecting the computed favorable electronic binding energies for Li complexation.

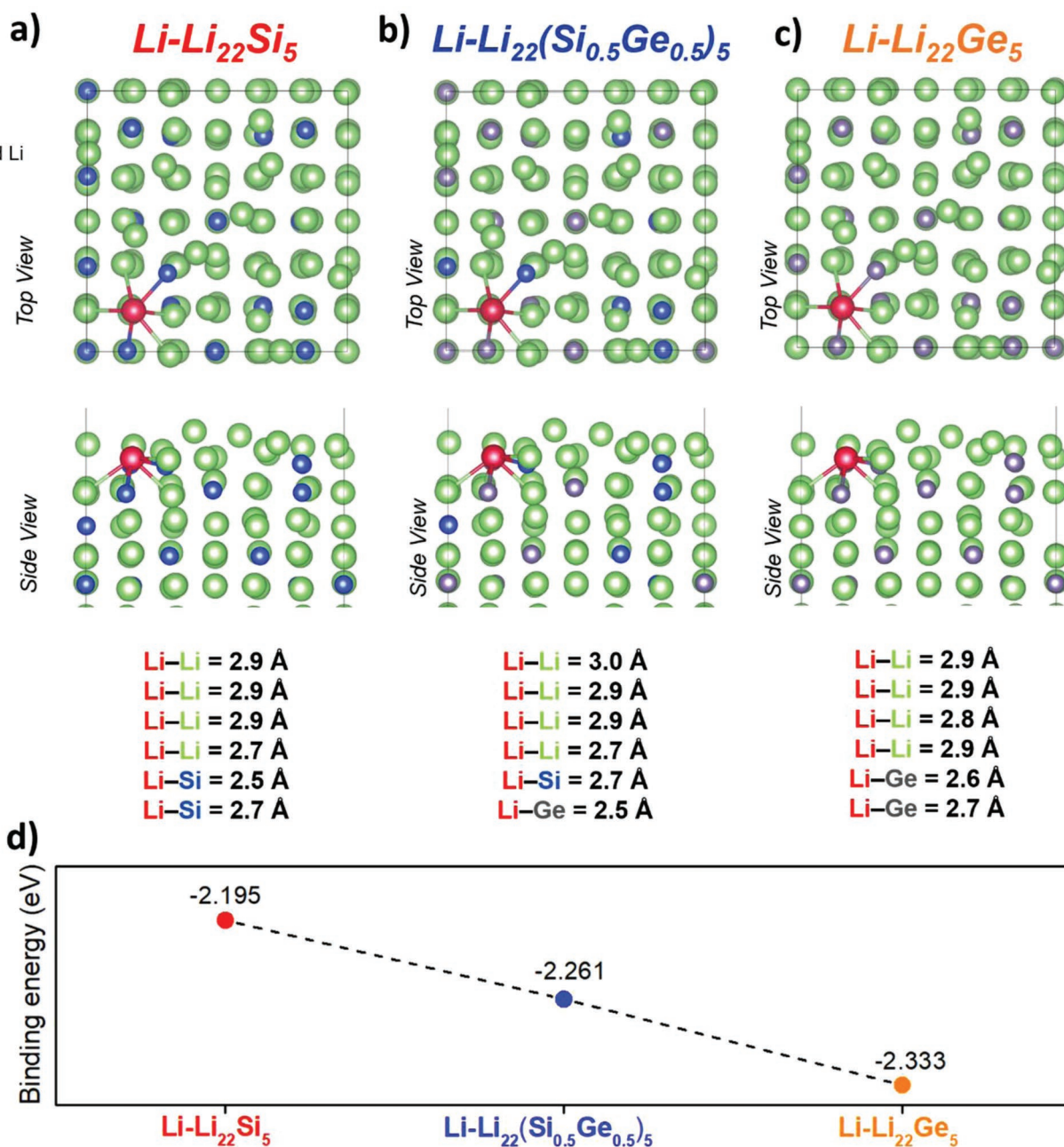


Figure 5. DFT-computed most stable Li-bound structures (top and side views) on the (110) surface of a) $Li_{22}Si_5$, b) $Li_{22}Ge_5$, and c) $Li_{22}(Si_{0.5}Ge_{0.5})_5$, with their corresponding bond lengths and d) binding energies, E_b .

2.5. Cell Performance in Li-Sulfur and Li-Metal Batteries

To demonstrate the practical use of the hosted Li metal anodes, we tested them in battery cells with sulfur and $LiFePO_4$ (LFP) cathodes. When paired with sulfur, the CP-LiGe/Li delivered a specific capacity of 835 mAh g^{-1} after 200 cycles at 0.5 C with a near perfect average coulombic efficiency ($\approx 99.94\%$). In contrast, CP-LiSi/Li-S, CP-LiSiGe/Li-S and pristine Li-S delivered lower capacities of 588, 668, and 498 mAh g^{-1} after 200 cycles with lower coulombic efficiencies of 96%, 98%, and 92%, respectively (Figure 6a). The specific capacity fluctuations

observed in full cells are due to temperature fluctuations ($22 \text{ C} \pm 4 \text{ }^\circ\text{C}$) in the lab during battery cycling which may have impacted Li-ion diffusivity through the SEI layer.^[56,57] A comparison of their voltage-capacity plots at 10th, 100th, and 200th cycle shows minimum overpotentials for the CP-LiGe/Li anode even with the increasing number of cycles at 0.5 C as compared to the other compositions and pristine Li (Figure S20, Supporting Information). The higher capacity retention of CP-LiGe/Li-S (82%) as compared to bare Li-S (73%) and other compositions at 0.5 C indicates the most stable plating/stripping behavior of CP-LiGe/Li anode during cycling in a sulfur

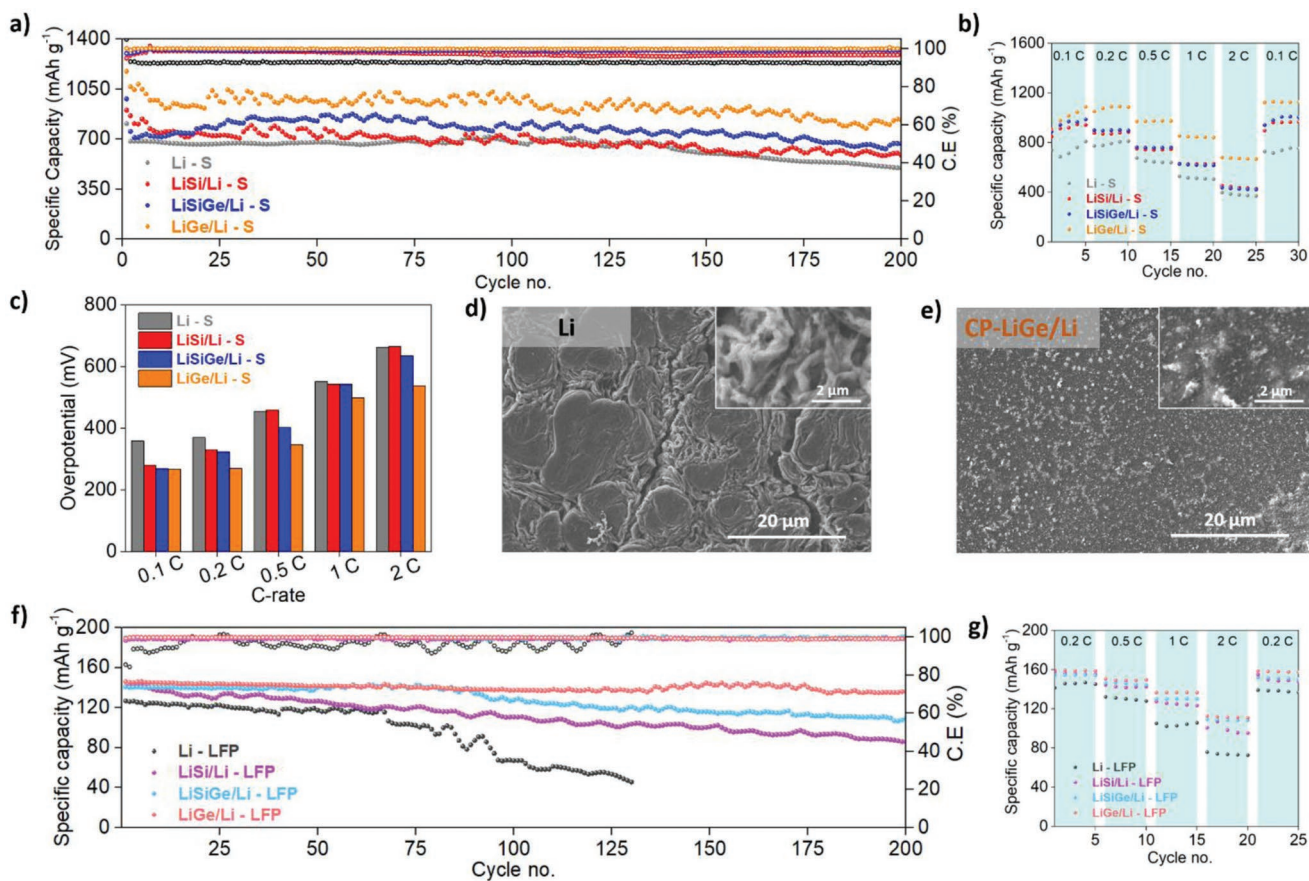


Figure 6. Effect of different metal anode NW (CP-LiSi/Li, CP-LiSiGe/Li, CP-LiGe/Li) substrates in Li-S and Li-LFP batteries. a) Cyclic performance of Li-S battery at 0.5 C. b) Rate capability test at various C-rates of 0.1 C, 0.2 C, 0.5 C, 1 C, and 2 C. c) Corresponding overpotential versus C-rate graph presenting overpotentials at various C-rates in Li-S battery. SEM analysis of d) Li anode and e) CP-LiGe/Li anode post 200 cycles cycled in a Li-S cell at 0.5 C. f) cyclic performance of Li-LFP battery at 0.5 C. g) Rate capability test at various C-rates of 0.2 C, 0.5 C, 1 C and 2 C in Li-LFP battery.

battery. As a result, a technologically relevant rate performance of 1009, 1076, 971, 847, and 676 mAhg^{-1} was obtained at 0.1, 0.2, 0.5, 1, and 2 C respectively (Figure 6b). In comparison, CP-LiSi/Li-S, CP-LiSiGe/Li-S, and bare Li-S cells delivered much lower specific capacity values at similar C-rates. The bare Li-S cell delivered 686, 777, 652, 517, and 396 mAh g^{-1} specific capacity at 0.1 C, 0.2 C, 0.5 C, 1 C, and 2 C respectively, affirming that the bare Li anode delivers the lowest capacity among all the compositions tested. A comparison of overpotentials suggests that Li metal followed by CP-LiSi/Li maintains the highest overpotential during cycling at various C-rates. Due to the most uniform deposition-stripping behavior among other compositions, the overpotentials are lowest for CP-LiGe/Li substrate with 267, 270, 346, 499, and 538 mV at 0.1, 0.2, 0.5, 1, and 2 C respectively (Figure 6c and Figure S21, Supporting Information). The post-mortem SEM of the Li anode extracted after 200 cycles (at 0.5 C) reveals the deposition of Li metal lumps with the formation of Li dendrites among cracks during cycling. The Li dendrites cause poor ionic transport, resulting in low specific capacities and low coulombic efficiencies as compared to the CP-LiGe/Li-S cell. The CP-LiGe/Li anode extracted from the S cell shows relatively uniform surface coverage with no dendrites, consistent with its robust performance in a CP-LiGe/Li-S cell (Figure 6d,e).

Since LiFePO_4 is among the most mature cathode material candidates for next-generation rechargeable Li-based batteries (Li-ion and LMBs),^[58–60] we tested a pristine Li anode along with CP-LiSi/Li, CP-LiSiGe/Li, and CP-LiGe/Li anodes against a LFP cathode. The cycling stability at 0.5 C shows that the pristine Li anode had the lowest cycling stability, with fluctuating coulombic efficiency during cycling (Figure 6f). The CP-LiSi/Li, CP-LiSiGe/Li, and CP-LiGe/Li batteries all started with similar specific capacities and, after 200 cycles, the CP-LiSi/Li-LFP, CP-LiSiGe/Li-LFP and CP-LiGe/Li-LFP delivered capacities of 86, 109, and 136 mAh g^{-1} with a capacity retention of 60%, 78%, and 93% respectively. The highest capacity retention in the case of CP-LiGe/Li metal anode confirms that the CP-LiGe/Li can act as a robust Li reservoir for LFP cathode with high coulombic efficiency. The voltage-specific capacity graphs of various anodes after 1st, 10th, and 100th cycle are shown in Figure S22, Supporting Information. Furthermore, the rate capability test demonstrates that the specific capacity tested at 0.2, 0.5, 1, and 2 C shows a similar trend, where the lowest capacity was obtained for the pristine Li anode while the highest specific capacity was obtained for the CP-LiGe/Li-LFP cell (Figure 6g). The corresponding voltage-capacity profiles are shown in Figure S23, Supporting Information. The CP-LiGe/Li-LFP cell delivered 160, 149, 136, and 113 mAh g^{-1} as compared to 142,

132, 110, and 82 mAh g⁻¹ in pristine Li-LFP cell at 0.2, 0.5, 1, and 2 C respectively. Finally, high-loading NMC811 cathodes (10 mg cm⁻²) was also tested to compare the performance of the best-performing anode (i.e., CP-LiGe/Li) with bare Li metal. The cycling performance clearly shows that CP-LiGe/Li-NMC outperformed the Li-NMC cell tested at 0.5 C over 200 cycles (Figure S24a, Supporting Information). The CP-LiGe/Li-NMC cell maintained 99.4% coulombic efficiency with a high-capacity retention of 90.2% (148 mAh g⁻¹ – 1st cycle, 133.5 mAh g⁻¹ – 200th cycle) after 200 cycles. The voltage-specific capacity graphs (Figure S24b,c, Supporting Information) also shows high voltage stability in CP-LiGe/Li-NMC cell as compared to Li-NMC cells, which further proves the benefits of using highly lithiophilic CP-LiGe/Li anode compared to Li metal.

3. Conclusion

We successfully designed a Li host architecture based on lithiophilic NWs (Si, SiGe alloy, and Ge) grown on a 3D carbon substrate, removing the obstacles of instability and performance decrease for LMBs. All three NW compositions enabled Li infiltration into the CP substrate, while also being converted into lithiated phases that mediated Li plating/stripping. In comparison to Si and SiGe alloy NWs, Ge NW coated substrates facilitated the most uniform Li plating/stripping during cycling, reflecting the higher lithiophilicity of Ge versus Si as substantiated by DFT models. Additionally, because of the uniform localized current density provided by the NW morphology of the lithiated phases, the CP-LiSi/Li, CP-LiSiGe/Li, and CP-LiGe/Li metal anodes demonstrated lower overpotentials than pristine Li anodes, with CP-LiGe/Li delivering the lowest overpotential of 40 mV after 1000 h at 1 mA cm⁻². When cycled as practical LMBs with sulfur, LFP, and NMC811 cathodes, the CP-LiGe/Li anode demonstrated 82%, 93%, and 90% capacity retention at 0.5 C after 200 cycles. This work opens up new avenues for the use of lithiophilic NW materials to suppress Li dendrite formation, allowing uniform Li deposition and unlocking cycling stability for long-life, high ED LMBs. Future investigations will focus on the chemical nature and evolution of the SEI on the different hosted anode structures as a function of cycle number.

Supporting Information

Supporting Information is available from the Wiley Online Library or from the author.

Acknowledgements

This project was supported by Science Foundation Ireland under grant no. 18/SIRG/5484. D.T. acknowledges support from Science Foundation Ireland (SFI) under award number 12/RC/2275_P2 and supercomputing resources at the SFI/Higher Education Authority Irish Center for High-End Computing (ICHEC). The authors would like to thank Dr. Fathima Laffir (Bernal Institute instrument scientist) for help with XPS analysis.

Open access funding provided by IReL.

Conflict of Interest

The authors declare no conflict of interest.

Data Availability Statement

The data that support the findings of this study are available from the corresponding author upon reasonable request.

Keywords

carbon frameworks, Li metal, lithiophilic, nanowires

Received: August 22, 2022

Revised: November 3, 2022

Published online:

- [1] D. Lin, Y. Liu, Y. Cui, *Nat. Nanotechnol.* **2017**, *12*, 194.
- [2] C. P. Grey, D. S. Hall, *Nat. Commun.* **2020**, *11*, 2.
- [3] X. B. Cheng, R. Zhang, C. Z. Zhao, Q. Zhang, *Chem. Rev.* **2017**, *117*, 10403.
- [4] R. Wang, W. Cui, F. Chu, F. Wu, *J. Energy Chem.* **2020**, *48*, 145.
- [5] J. H. Um, K. Kim, J. Park, Y. E. Sung, S. H. Yu, *J. Mater. Chem. A* **2020**, *8*, 13874.
- [6] L. Trahey, F. R. Brushett, N. P. Balsara, G. Ceder, L. Cheng, Y. M. Chiang, N. T. Hahn, B. J. Ingram, S. D. Minter, J. S. Moore, K. T. Mueller, L. F. Nazar, K. A. Persson, D. J. Siegel, K. Xu, K. R. Zavadil, V. Srinivasan, G. W. Crabtree, *Proc. Natl. Acad. Sci. USA* **2020**, *117*, 12550.
- [7] P. G. Bruce, S. A. Freunberger, L. J. Hardwick, J. M. Tarascon, *Nat. Mater.* **2012**, *11*, 19.
- [8] J. Lu, L. Li, J. B. Park, Y. K. Sun, F. Wu, K. Amine, *Chem. Rev.* **2014**, *114*, 5611.
- [9] F. Wu, Y. X. Yuan, X. B. Cheng, Y. Bai, Y. Li, C. Wu, Q. Zhang, *Energy Storage Mater.* **2018**, *15*, 148.
- [10] Z. A. Ghazi, Z. Sun, C. Sun, F. Qi, B. An, F. Li, H. M. Cheng, *Small* **2019**, *15*, 1900687.
- [11] W. Xu, J. Wang, F. Ding, X. Chen, E. Nasybulin, Y. Zhang, J. G. Zhang, *Energy Environ. Sci.* **2014**, *7*, 513.
- [12] C. Wei, Y. Zhang, Y. Tian, L. Tan, Y. An, Y. Qian, B. Xi, S. Xiong, J. Feng, Y. Qian, *Energy Storage Mater.* **2021**, *38*, 157.
- [13] Z. Yu, Y. Cui, Z. Bao, *Cell Rep* **2020**, *1*, 100119.
- [14] X. Shen, R. Zhang, X. Chen, X. B. Cheng, X. Li, Q. Zhang, *Adv. Energy Mater.* **2020**, *10*, 1903645.
- [15] M. D. Tikekar, S. Choudhury, Z. Tu, L. A. Archer, *Nat. Energy* **2016**, *1*, 16114.
- [16] V. Nilsson, A. Kotronia, M. Lacey, K. Edström, P. Johansson, *ACS Appl. Energy Mater.* **2020**, *3*, 200.
- [17] D. Luo, M. Li, Y. Zheng, Q. Ma, R. Gao, Z. Zhang, H. Dou, G. Wen, L. Shui, A. Yu, X. Wang, Z. Chen, *Adv. Sci.* **2021**, *8*, 2101051.
- [18] J. Qian, W. A. Henderson, W. Xu, P. Bhattacharya, M. Engelhard, O. Borodin, J.-G. Zhang, *Nat. Commun.* **2015**, *6*, 6362.
- [19] S. S. Zhang, *Electrochim. Acta* **2012**, *70*, 344.
- [20] S. S. Zhang, *J. Power Sources* **2016**, *322*, 99.
- [21] T. Li, X. Q. Zhang, P. Shi, Q. Zhang, *Joule* **2019**, *3*, 2647.
- [22] S. Chen, Y. Xiang, G. Zheng, Y. Liao, F. Ren, Y. Zheng, H. He, B. Zheng, X. Liu, N. Xu, M. Luo, J. Zheng, Y. Yang, *ACS Appl. Mater. Interfaces* **2020**, *12*, 27794.
- [23] X. Wang, Y. Tan, G. Shen, S. Zhang, *J. Energy Chem.* **2020**, *41*, 149.
- [24] Y. Zheng, N. Yang, R. Gao, Z. Li, H. Dou, G. Li, L. Qian, Y. Deng, J. Liang, L. Yang, Y. Liu, Q. Ma, D. Luo, N. Zhu, K. Li, X. Wang, Z. Chen, *Adv. Mater.* **2022**, *2203417*, 2203417.

- [25] Y. Jiang, Y. Song, X. Chen, H. Wang, L. Deng, G. Yang, *Energy Storage Mater.* **2022**, 52, 514.
- [26] H. Dai, X. Gu, J. Dong, C. Wang, C. Lai, S. Sun, *Nat. Commun.* **2020**, 11, 643.
- [27] F. Liu, L. Wang, Z. Zhang, P. Shi, Y. Feng, Y. Yao, S. Ye, H. Wang, X. Wu, Y. Yu, *Adv. Funct. Mater.* **2020**, 30, 2001607.
- [28] C. Yan, X. B. Cheng, Y. Tian, X. Chen, X. Q. Zhang, W. J. Li, J. Q. Huang, Q. Zhang, *Adv. Mater.* **2018**, 30, 1707629.
- [29] D. Kang, N. Hart, J. Koh, L. Ma, W. Liang, J. Xu, S. Sardar, J. P. Lemmon, *Energy Storage Mater.* **2020**, 24, 618.
- [30] C. P. Yang, Y. X. Yin, S. F. Zhang, N. W. Li, Y. G. Guo, *Nat. Commun.* **2015**, 6, 8058.
- [31] Q. Yun, Y. B. He, W. Lv, Y. Zhao, B. Li, F. Kang, Q. H. Yang, *Adv. Mater.* **2016**, 28, 6932.
- [32] L. L. Lu, J. Ge, J. N. Yang, S. M. Chen, H. Bin Yao, F. Zhou, S. H. Yu, *Nano Lett.* **2016**, 16, 4431.
- [33] L. L. Lu, Y. Zhang, Z. Pan, H. Bin Yao, F. Zhou, S. H. Yu, *Energy Storage Mater.* **2017**, 9, 31.
- [34] W. Tang, X. Yin, S. Kang, Z. Chen, B. Tian, S. L. Teo, X. Wang, X. Chi, K. P. Loh, H. W. Lee, G. W. Zheng, *Adv. Mater.* **2018**, 30, 1801745.
- [35] H. Wang, X. Cao, H. Gu, Y. Liu, Y. Li, Z. Zhang, W. Huang, H. Wang, J. Wang, W. Xu, J. G. Zhang, Y. Cui, *ACS Nano* **2020**, 14, 4601.
- [36] H. Wang, D. Lin, Y. Liu, Y. Li, Y. Cui, *Sci. Adv.* **2017**, 3, e170130.
- [37] Z. Liang, D. Lin, J. Zhao, Z. Lu, Y. Liu, C. Liu, Y. Lu, H. Wang, K. Yan, X. Tao, Y. Cui, *Proc. Natl. Acad. Sci. USA* **2016**, 113, 2862.
- [38] Y. Zhang, C. Wang, G. Pastel, Y. Kuang, H. Xie, Y. Li, B. Liu, W. Luo, C. Chen, L. Hu, *Adv. Energy Mater.* **2018**, 8, 1800635.
- [39] X. Y. Yue, X. L. Li, W. W. Wang, D. Chen, Q. Q. Qiu, Q. C. Wang, X. J. Wu, Z. W. Fu, Z. Shadik, X. Q. Yang, Y. N. Zhou, *Nano Energy* **2019**, 60, 257.
- [40] Y. Liu, D. Lin, Z. Liang, J. Zhao, K. Yan, Y. Cui, *Nat. Commun.* **2016**, 7, 10992.
- [41] S. Abdul Ahad, S. Kilian, M. Zubair, V. A. Lebedev, K. McNamara, K. M. Ryan, T. Kennedy, H. Geaney, *J. Mater. Chem. A* **2021**, 9, 20626.
- [42] K. Stokes, H. Geaney, G. Flynn, M. Sheehan, T. Kennedy, K. M. Ryan, *ACS Nano* **2017**, 11, 10088.
- [43] Q. Wang, W. Ren, F. Gao, C. Qiu, Q. Wang, F. Gao, C. Zhao, *ChemElectroChem* **2019**, 1768.
- [44] K. V. Greco, A. Forner-Cuenca, A. Mularczyk, J. Eller, F. R. Brushett, *ACS Appl. Mater. Interfaces* **2018**, 10, 44430.
- [45] R. Zhang, X. Chen, X. Shen, X. Q. Zhang, X. R. Chen, X. B. Cheng, C. Yan, C. Z. Zhao, Q. Zhang, *Joule* **2018**, 2, 764.
- [46] P. Shi, T. Li, R. Zhang, X. Shen, X. B. Cheng, R. Xu, J. Q. Huang, X. R. Chen, H. Liu, Q. Zhang, *Adv. Mater.* **2019**, 31, 1807131.
- [47] J. Zhao, J. Sun, A. Pei, G. Zhou, K. Yan, Y. Liu, D. Lin, Y. Cui, *Energy Storage Mater.* **2018**, 10, 275.
- [48] S. Li, Q. Liu, J. Zhou, T. Pan, L. Gao, W. Zhang, L. Fan, Y. Lu, *Adv. Funct. Mater.* **2019**, 29, 1808847.
- [49] J. Pu, J. Li, K. Zhang, T. Zhang, C. Li, H. Ma, J. Zhu, P. V. Braun, J. Lu, H. Zhang, *Nat. Commun.* **2019**, 10, 1896.
- [50] H. Zhang, X. Liao, Y. Guan, Y. Xiang, M. Li, W. Zhang, X. Zhu, H. Ming, L. Lu, J. Qiu, Y. Huang, G. Cao, Y. Yang, L. Mai, Y. Zhao, H. Zhang, *Nat. Commun.* **2018**, 9, 3729.
- [51] C. Wei, L. Tan, Y. Tao, Y. An, Y. Tian, H. Jiang, J. Feng, Y. Qian, *Energy Storage Mater.* **2021**, 34, 12.
- [52] C. Y. Chou, G. S. Hwang, *J. Power Sources* **2014**, 263, 252.
- [53] P. R. Abel, A. M. Chockla, Y. M. Lin, V. C. Holmberg, J. T. Harris, B. A. Korgel, A. Heller, C. B. Mullins, *ACS Nano* **2013**, 3, 2249.
- [54] G. Kresse, J. Hafner, *Phys. Rev. B* **1994**, 49, 14251.
- [55] G. Kresse, J. Furthmüller, *Comput. Mater. Sci.* **1996**, 6, 15.
- [56] S. Kilian, K. McCarthy, K. Stokes, T. E. Adegoke, M. Conroy, I. S. Amiinu, H. Geaney, T. Kennedy, K. M. Ryan, *Small* **2021**, 17, 2005443.
- [57] T. Kennedy, M. Brandon, F. Laffir, K. M. Ryan, *J. Power Sources* **2017**, 359, 601.
- [58] J. Li, Z.-F. Ma, *Chem* **2019**, 5, 3.
- [59] A. Manthiram, *Nat. Commun.* **2020**, 11, 1550.
- [60] X. G. Yang, T. Liu, C. Y. Wang, *Nat. Energy* **2021**, 6, 176.